First results of the glitching pulsars monitoring program at the Argentine Institute of Radioastronomy

Ezequiel Zubieta[1★], Ryan Missel[2], Valentina Sosa Fiscella[1,4], Carlos O. Lousto[3,4†], Santiago del Palacio[1,6], Federico G. López Armengol[4], Federico García[1,5], Jorge A. Combi[1,5], Linwei Wang[2], Luciano Combi[1,4], Guillermo Gancio[1], Carolina Negrelli[5], Eduardo M. Gutiérrez[1]

[1]Instituto Argentino de Radioastronomía (CCT La Plata, CONICET; CICPBA; UNLP), C.C.5, (1894) Villa Elisa, Buenos Aires, Argentina.
[2]Golisano College of Computing and Information Sciences, Rochester Institute of Technology Rochester, NY 14623, USA
[3]School of Mathematical Sciences, Sciences Rochester Institute of Technology Rochester, NY 14623, USA
[4]Center for Computational Relativity and Gravitation, Rochester Institute of Technology, 85 Lomb Memorial Drive, Rochester,New York 14623, USA
[5]Facultad de Ciencias Astronómicas y Geofísicas, Universidad Nacional de La Plata, Paseo del Bosque, B1900FWA La Plata, Argentina
[6]Department of Space, Earth and Environment, Chalmers University of Technology, SE-412 96 Gothenburg, Sweden

Accepted XXX. Received YYY; in original form ZZZ

ABSTRACT

We report here on the first results of a systematic monitoring of southern glitching pulsars at the Argentine Institute of Radio astronomy started on the year 2019. We detected a major glitch in the Vela pulsar (PSR J0835−4510) and two mini-glitches in PSR J1048−5832. For each glitch, we present the measurement of glitch parameters by fitting timing residuals.We then make an individual pulses study of Vela in observations previous and after the glitch. We selected 6 days of observations around the major glitch on July 22nd 2021 and study their statistical properties with machine learning techniques. We use Variational AutoEncoder (VAE) reconstruction of the pulses to separate them clearly from the noise. We perform a study with Self-Organizing Maps (SOM) clustering techniques and find an unusual behavior of the clusters two days prior to the glitch. This behavior is only visible in the the higher amplitude pulse clusters and if intrinsic to the pulsar could be interpreted as a precursor of the glitch.

Key words: pulsars: Vela – methods: observational – methods: statistical

1 INTRODUCTION

Pulsars are a sub-type of neutron stars that present pulsed emission, predominantly in the radio band. The very high moment of inertia of the neutron stars renders them with an extraordinarily stable rotation, making pulsars one of the most accurate clocks in the Universe. Although pulsars have extremely stable periods over time, some young pulsars are prone to have glitches: sudden changes in their period due to changes in the interior of the star. Discovered 50 years ago, nowadays almost 200 pulsars are known to glitch (Manchester 2018). Southern (Yu et al. 2013) and northern (Espinoza et al. 2011; Fuentes et al. 2017) based surveys provide comprehensive catalogs such as ATNF[1]. The physical mechanism behind these glitches is still not well understood.

The Vela Pulsar (PSR B0833−45/J0835−4510) is one of the most active pulsars in terms of glitching, counting 21 in the last 50+ years. Although erratic, this pulsar exhibits major glitches every 2–3 years. On the theoretical modeling, superfluidity is required to explain the large Vela glitches (Andersson et al. 2012; Haskell & Melatos 2015), with the glitch magnitude giving some idea of the available angular momentum reservoir (how much of the star is superfluid). Observations can also be used to estimate the mass of the neutron stars (Ho et al. 2015; Montoli et al. 2020; Khomenko & Haskell 2018) and the post-glitch relaxation properties should provide a handle on the so-called mutual friction (involving vortices). Moreover, a detailed study of the pulsed emission can provide further insight on the physics of glitches. In particular, the analysis of the single pulses in the 2016 Vela glitch showed an atypical behaviour of a few pulses around the glitch, including a null, which revealed that the glitch also affects the pulsar magnetosphere (Palfreyman et al. 2018). Unfortunately, the unpredictable character of the glitch phenomenon makes it extremely difficult to observe. A valid question is whether it is possible that information of a glitch precursor exists before the glitch event itself, and also if we can learn more from observations during the relaxation phase just after the glitch.

Since 2019, the Pulsar Monitoring in Argentina[2] (PuMA) collaboration has been monitoring with high cadence a set of pulsars

★ Fellow of CONICET, Argentina. E-mail: ezubieta@iar.unlp.edu.ar
† E-mail: colsma@rit.edu (COL)

[1] http://www.atnf.csiro.au/people/pulsar/psrcat/glitchTbl.html
http://www.jb.man.ac.uk/pulsar/glitches/gTable.html

[2] https://puma.iar.unlp.edu.ar

from the southern hemisphere that had shown glitches before (Gancio et al. 2020). The observations are carried out with the antennas from the Argentine Institute of Radio astronomy (IAR). A major goal of our observing campaign is the close follow-up of the Vela pulsar. The consistency of our monitoring allowed us to detect its last two glitches: the one on Feb 1st 2019 (Lopez Armengol et al. 2019) was measured with observations three days before and three days after the event, while the one on July 2021 (Sosa-Fiscella et al. 2021) was observed just one hour after the glitch. We plan to continue monitoring the Vela pulsar to attempt to capture a glitch "live" during our 3.5-h daily observations.

Moreover, as the Vela pulsar is very bright, we are able to detect its individual (single) pulses. Recently, in Lousto et al. (2021) we performed an individual-pulses study of a sample of our daily observations that span over three hours (around 120,000 pulses per observation). We selected 4 days of observations in January–March 2021 and studied their statistical properties with machine learning techniques. We first used density based DBSCAN clustering techniques, associating pulses mainly by amplitudes, and found a correlation between higher amplitudes and earlier arrival times. We also found a weaker (polarization dependent) correlation with the mean width of the pulses. We identified clusters of the so-called mini-giant pulses, with ~ 10 times the average pulse amplitude. We then performed an independent study, using the Variational AutoEncoder (VAE) reconstruction of the pulses to separate them clearly from the noise and select one of the days of observation to train VAE and apply it to the rest of the observations. We applied to those reconstructed pulses Self-Organizing Maps (SOM) clustering techniques to determine 4 clusters of pulses per day per radio telescope and concluded that our main results were robust and self-consistent. These results supported models for emitting regions at different heights (separated each by roughly a hundred km) in the pulsar magnetosphere. Given the success of these techniques we apply them here on the major glitch event on July 22nd 2021, for which we have collected data daily around that glitch.

The goals of our observing campaign also include the creation of updated ephemeris of glitching pulsars that can be relevant for other studies, such as the search of continuous gravitational waves detectors such as LIGO. In addition to Vela, we are currently monitoring the pulsars mentioned in Gancio et al. (2020), J0738−4042, J0742−2822, J1048−5832 J1430−6623, J1644−4559, J1709−4429, J1721−3532, J1731−4744, J1740−3015, and plan to extend the list to other accessible (bright) glitching pulsars. In this work we present our observations of the pulsars J0835−4510 and J1048−5832 and provide a detailed analysis of their most recent glitches. We find a large Vela glitch on July 22nd 2021 and two mini-glitches (the lowest amplitude so far from the previous 7 glitches recorded) on December 20th 2020 and on November 20th 2021.

2 PULSARS GLITCH MONITORING PROGRAM AT IAR

The IAR observatory is located near the city of La Plata, Argentina (local time UTC−3), at latitude $-34°51'57''.35$ and longitude $58°08'25''.04$. It has two 30 m single-dish antennas, A1 and A2, aligned on a North–South direction and separated by 120 m. These radio telescopes cover a declination range of $-90° < \delta < -10°$ and an hour angle range of two hours east/west, $-2\,\mathrm{h} < t < 2\,\mathrm{h}$. Although the IAR is not located in a radio frequency interferences (RFI) quiet zone, the analysis of the RFI environment presented in Gancio et al. (2020) showed that the radio band from 1 GHz to 2 GHz has a low level of RFI activity that is suitable for radio astronomy.

Major upgrades have been developed in both antennas since 2014. Some of these include the installation of two digitizer boards of 56 MHz bandwidth that can be used as consecutive bands to give a total 112-MHz bandwidth on a single polarization. We note that the receiver in A2 is different from the one in A1, having fewer radio frequency components and larger RF bandwidth, which translates in different responses for each antenna. A detailed description of the characteristics of the current front end in A1 and A2 are given in Gancio et al. (2020). We highlight that a major asset of IAR's observatory is its availability for high-cadence long-term monitoring of bright sources.

We are carrying out an intensive monitoring campaign of known bright glitching pulsars in the southern hemisphere in the L-band (1400 MHz) using the two IAR antennas. Our observational program includes high-cadence observations (up to daily) with a duration of up to 3.5 h per day. This builds a unique database aimed to detect and characterise both large and small (mini-) glitches. In addition, the intensive monitoring also gives a significant chance that a glitch could be observed "live", a goal that has been achieved only on extremely rare occasions by other monitoring programs (Palfreyman et al. 2018).

For both antennas, the data is acquired with a timing resolution of 146 μs. In the case of A1, we use 128 channels of 0.875 MHz centered at 1400 MHz in single (circular) polarization mode, whereas for A2 we use 64 channels of 1 MHz centered at 1416 MHz and in dual polarization (both circular polarizations added). When possible, we observe each target with both antennas independently, in order to control systematic effects. Unfortunately, a clock issue affected the observations with A2 during the period MJD 59400–59435 (July 5th to August 9th, 2022), which thus had to be excluded in the timing analysis of the residuals.

Here we analyse close to 270 h of data of Vela J0835−4510 (145.6 h with A1, 122.7 h with A2) taken in the period (MJD) 59371–59463. These observations include an almost daily monitoring close to the 2021 glitch (Sect. 3.2). In addition, we also study 730 h of data of J1048−5832 (553.7 h with A1, 177.3 h with A2) during the period (MJD) 59031–59729. We note that, when possible, the observations of the Vela pulsar span for the maximum tracking range of the antennas, which is ~ 3.5 h, while for J1048−5832 they last < 2.5 h, due to an overlap with Vela (which is prioritized in our schedule).

3 GLITCHES: ANALYSIS AND RESULTS

Pulsar rotation can be monitored by observing the times of arrival (ToAs) of their pulses. To extract information from the ToAs, one introduces a timing model that is essentially a mathematical model aimed to predict the ToAs. The difference between the predicted and observed ToAs can reveal the limitations of the timing model to represent the pulsar behaviour, which can be used to derive information of the pulsar itself.

In the timing model, the temporal evolution of the pulsar phase is modeled as a Taylor expansion (Basu et al. 2021),

$$\phi(t) = \phi + \nu(t - t_0) + \frac{1}{2}\dot{\nu}(t - t_0)^2 + \frac{1}{6}\ddot{\nu}(t - t_0)^3, \quad (1)$$

where ν, $\dot{\nu}$ and $\ddot{\nu}$ are the rotation frequency of the pulsar, and its first and second derivatives.

When a glitch occurs, the pulsar suffers a sudden jump in its rotation frequency. This spin up can be introduced in the timing model as a change in the phase of the pulsar modeled as (Mcculloch et al. 1987)

$$\phi_g(t) = \Delta\phi + \Delta\nu_p(t - t_g) + \frac{1}{2}\Delta\dot{\nu}_p(t - t_g)^2 + \frac{1}{6}\Delta\ddot{\nu}(t - t_g)^3 + \left[1 - \exp\left(-\frac{t - t_g}{\tau_d}\right)\right]\Delta\nu_d\,\tau_d, \quad (2)$$

where $\Delta\phi$ is the offset in pulsar phase, t_g is the glitch epoch, and $\Delta\nu_p$, $\Delta\dot{\nu}_p$ and $\Delta\ddot{\nu}$ are the respective permanents jumps in ν, $\dot{\nu}$ and $\ddot{\nu}$ relative to the pre-glitch solution. Finally, $\Delta\nu_d$ is the transient increment in the frequency that decays on a timescale τ_d. From these parameters one can calculate the degree of recovery, Q, which relates the transient and permanent jumps in frequency as $Q = \Delta\nu_d/\Delta\nu_g$. At last, two commonly used parameters in the literature are the changes in the pulse frequency and its first derivative, which can be described as

$$\Delta\nu_g = \Delta\nu_p + \Delta\nu_d \quad (3)$$

$$\Delta\dot{\nu}_g = \Delta\dot{\nu}_p - \frac{\Delta\nu_d}{\tau_d}\,. \quad (4)$$

The initial sets of parameters for the timing models were retrieved from the ATNF pulsar catalogue (Manchester et al. 2005), and then updated by ourselves. For the data reduction we used the software `presto` (Ransom et al. 2003; Ransom 2011). In particular, we used the tasks `rficlean` to remove RFIs and `prepfold` for folding the observations. The ToAs were subsequently determined from the folded observations using the Fourier phase gradient-matching template fitting (Taylor 1992) implemented in the `pat` package in `psrchive` (Hotan et al. 2004). Given the similarities between A1 and A2, we used the same template for observations with either antenna without introducing additional error. The template was created by applying a smoothing wavelet method to the pulse profile of a high signal-to-noise observation not included in the posterior timing analysis. Finally, the timing residuals were calculated using the pulsar timing software package `Tempo2` (Hobbs et al. 2006) in a Python interface provided by `libstempo`[3].

3.1 Mini-glitches detection in PSR J1048-5832

PSR J1048−5832 has a period of 123 ms and a period derivative of 9.61×10^{-14} s s^{-1}, which leads to a characteristic age of about 20 kyr. In 2009, *Fermi*-LAT detected its gamma-ray pulsations (photon energies > 0.1 GeV), adding PSR J1048−5832 to the list of young gamma-ray pulsars in the Galactic plane (Abdo et al. 2009). In addition, an optical counterpart has been searched with deep VLT imaging in Danilenko et al. (2013), and periodic mode-changing has been revealed with high-sensitivity radio observations in Yan et al. (2020).

Seven glitches have been reported so far for this pulsar. Here, we report the detection of two more glitches on MJD 59203.9(5) (Zubieta et al. 2022) and MJD 59540(2). We used the `glitch` plug-in in `tempo2` (Hobbs et al. 2006) to subdivide the observations in blocks of 50–100 days and then fit ν_0 and $\dot{\nu}_0$ in each of these blocks. The results are displayed in Fig. 1. Our analysis reveals a frequency jump consistent with a glitch on MJD 59203.9, after which there is a continuous increase in the frequency relative to the pre-glitch model. This type of behaviour is unusual but it has also been observed in PSR J2219−4754 (Zhou et al. 2022) and PSR J0147+5922 (Yuan et al. 2010).

The dataset before the first glitch covers the timespan MJD 59031–59204 and accounts for 71 observations with A1 and 47 observations

[3] https://github.com/vallis/libstempo.

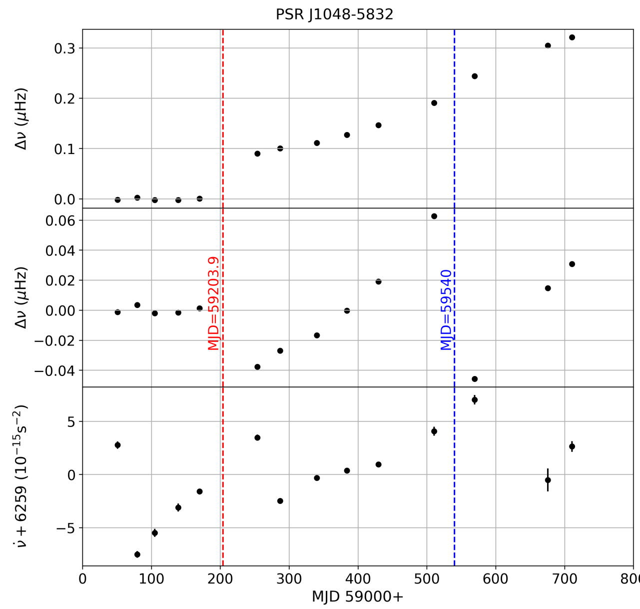

Figure 1. Timing analysis of PSR J1048−5832. *Top:* variations in the rotational frequency $\Delta\nu$ relative to the pre-glitch solution. *Center:* expanded plot of $\Delta\nu$, in which the mean post-glitch value has been subtracted from the post-glitch data. *Bottom:* variations of the frequency first derivative $\Delta\dot{\nu}$. The vertical dashed lines mark the epochs of the two glitches.

Table 1. Parameters of the timing model for PSR J1048−5832 and their 1σ uncertainties.

Parameter	Value (glitch 1)	Value (glitch 2)
PEPOCH (MJD)	59000	
F0(s^{-1})	8.08166079(4)	
F1(s^{-2})	$-6.2824(2) \times 10^{-12}$	
t_g (MJD)	59203.9(5)	59540(2)
$\Delta\phi$	~ 0	~ 0
$\Delta\nu_p(s^{-1})$	$7.19(7) \times 10^{-8}$	$8.02(25) \times 10^{-8}$
$\Delta\dot{\nu}_p(s^{-2})$	$3.91(9) \times 10^{-15}$	$1(2) \times 10^{-16}$

with A2. In the timespan between the first and the second glitch, MJD 59205–59513, we have 57 observations with A1 and 17 observations with A2. Finally, for the epoch after the second glitch, our dataset covers the timespan MJD 59571–59730, in which we have 16 observations with A1 and 16 observations with A2.

In Fig. 2 we show the timing residuals before and after the inclusion of the glitches in the timing model. This timing model is given by Eq. (1) and Eq. (2), and the fitted parameters are summarized in Table 1. No signs of exponential recovery were found for these glitches, so we do not include the exponential decay term in the final fitting. The white noise in the data was characterised using `TempoNest` via the parameters $TNGlobalEF$ and $TNGlobalEQ$. We performed a bayesian analysis in a short timespan in order to eliminate the effect of the red noise. We obtained $TNGlobalEF = 2.59$ and $TNGLobalEQ = -5.13$; the former indicates the factor by which the template-fitting underestimates the ToA errorbars, and the latter a systematic uncertainty of ≈ 7 μs.

In Table 2 we recompile the magnitude of all the previous glitches of PSR J1048−5832 and compare it with the values of the new glitches reported in this work (on December 20th 2020 and November

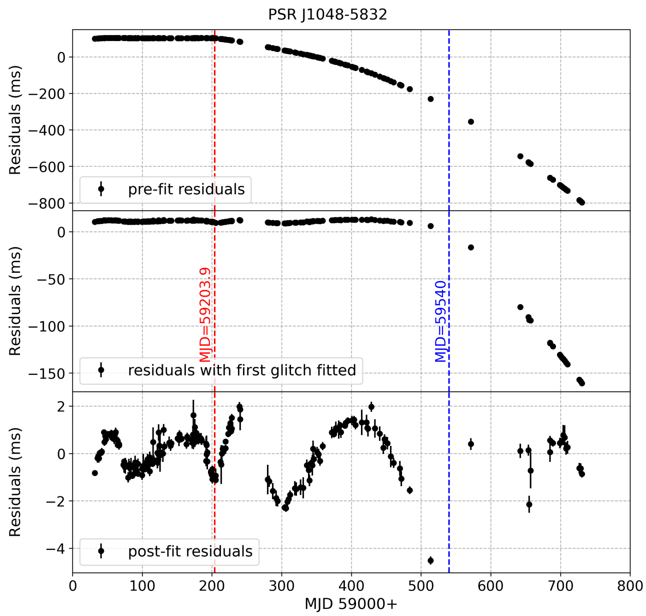

Figure 2. PSR J1048−5832 timing residuals for a timing model with no glitches (*top*), with the first glitch included (*middle*) and with the second glitch included (*bottom*). The epochs of the glitches are indicated with coloured vertical lines.

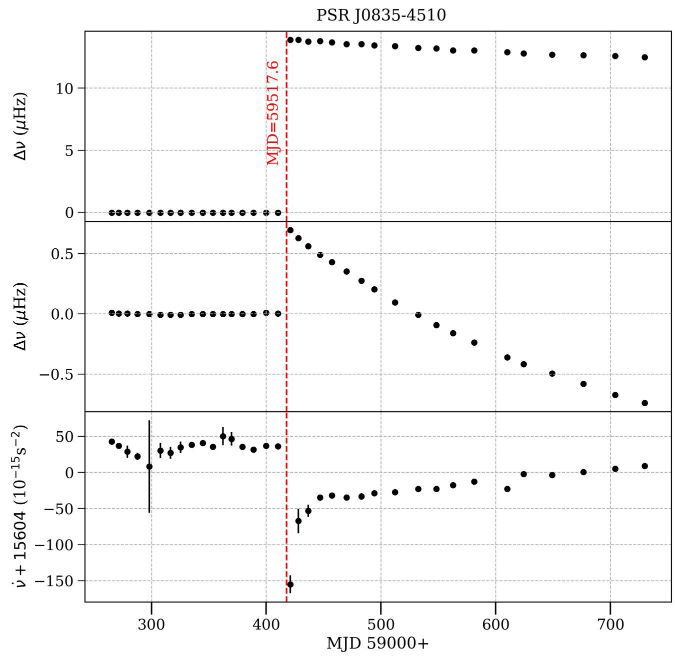

Figure 3. Vela's glitch: (top) variations in the rotational frequency $\Delta\nu$ relative to the pre-glitch solution, (center) an expanded plot of $\Delta\nu$, in which the mean post-glitch value has been subtracted from the post-glitch data, and (bottom) variations of the frequency first derivative $\Delta\dot{\nu}$. The vertical dashed line marks the glitch epoch.

Table 2. Magnitude of the glitches in PSR J1048−5832. The values for the previous glitches were extracted from the ATNF Catalog (Manchester et al. 2005).

MJD	$\Delta\nu_g/\nu$ (10^{-9})	References
48944(2)	25(2)	Wang et al. (2000)
49034(9)	2995(7)	Wang et al. (2000)
50788(3)	771(2)	Wang et al. (2000)
52733(37)	1838.4(5)	Yu et al. (2013)
53673.0(8)	28.5(4)	Yu et al. (2013)
54495(4)	3044.1(9)	Lower et al. (2021)
56756(4)	2964(3)	Lower et al. (2021)
59203.9(5)	8.89(9)	This work
59540(2)	9.9(3)	This work

20th 2021). These new glitches can be classified as mini-glitches given that they present values of $\Delta\nu_g/\nu \sim 10^{-8} \ll 10^{-6}$. We note that there were two mini-glitches previously detected in this pulsar, but even in these cases their amplitudes were ≈ 3 times larger than the ones of the two glitches reported in this work.

3.2 Glitch detection in PSR J0835-4510 (Vela)

We reported the detection of a new (#22) glitch in Vela in Sosa-Fiscella et al. (2021).We observed the Vela pulsar on Jul 21 for 165 min with A1 and 206 min with A2 (MJD 59416.6321–59416.7666). We measured a barycentric period of $P_{\rm bary} = 89.4086241(17)$ ms, consistent with the pulsar ephemeris at that time. No glitch was observed during that observation. In our following observation on Jul 22 (started in MJD 59417.6549) with A2, we obtained a period $P_{\rm bary} = 89.4065093(15)$ ms, showing a decrease of $\Delta P = 0.113\ \mu$s with respect to the expected period, which corresponds to $\Delta P/P = 1.26 \times 10^{-6}$. This result was confirmed with a subsequent observation on Jul 23 with A1 and A2. This first analysis placed the new Vela glitch between MJD 59416.7666–59417.6549. Subsequent reports (Dunn et al. 2021; Olney 2021; Singha et al. 2021) narrowed the glitch epoch to MJD 59417.618–59417.628.

Here we address a more thorough analysis of the Vela timing behaviour around the epoch of the glitch. In Fig. 5a) we show the residuals before including the glitch in the timing model. We focused on a time window of roughly 90 days centered in the glitch epoch (MJD 59417.6). During the pre-glitch window (MJD 59371.7–MJD 59416.7) our restricted dataset includes observations in 21 days with A1 and in 27 days with A2, while during the post-glitch window (MJD 59418.7—MJD 59463.6) we have observations in 30 days with A1 and in 23 days with A2.

We first derived the rotational parameters of the timing model before and after the glitch by fitting ν, $\dot{\nu}$ and $\ddot{\nu}$ in Eq. (1) to the pre-glitch and post-glitch data. For this we excluded the ToAs within 10 days after the glitch in order to avoid the effects of the strong exponential decay shown in Fig. 3. With the results for the pre-glitch solution and post-glitch asymptotic solution, we estimated the parameters $\Delta\nu_p$, $\Delta\dot{\nu}_p$ and $\Delta\ddot{\nu}$. The residuals after including and fitting these parameters in the timing model are shown in Fig. 5b).

The high cadence of observations of this pulsar makes it possible to monitor the recovery process rigorously. We used the glitch plugin in `TEMPO2` to obtain values of ν and $\dot{\nu}$ from individual sections of data, with each section spanning $\sim$ 10 d (Fig. 3). Both the glitch plugin and the timing residuals in Fig. 5b) clearly indicated a decaying term of a few days. We explored systematically the values of the decay timescale and looked for the value that led to the smallest $\chi^2_{\rm red}$ in the timing residuals. For each value of the decay constant, we fitted $\Delta\nu$, $\Delta\dot{\nu}$, $\Delta\ddot{\nu}$ and $\Delta\nu_d$, and obtained $\tau_d = 6.39(1)$ d. The residuals, shown in Fig. 5c), suggest the existence of an additional decay term. We therefore explored systematically the values of both decay timescales as explained before. The results are shown in Fig. 4, while the fitted

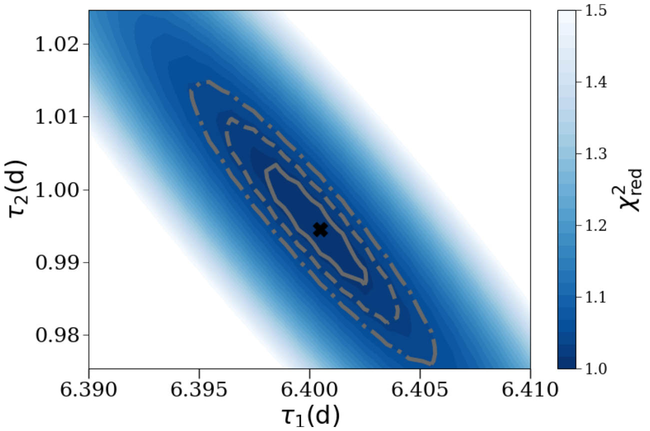

Figure 4. Best fit of the decay time constants τ_1 and τ_2 for the 2021 Vela glitch. The solid line, dashed line, and dot-dashed line indicate the 1-, 2- and 3-σ confidence regions.

Table 3. Parameters of the timing model for the July 22nd 2021 Vela glitch and their 1σ uncertainties.

Parameter	Value
PEPOCH (MJD)	59417.6193
F0(s^{-1})	11.18420841(1)
F1(s^{-2})	$-1.55645(4) \times 10^{-11}$
F2(s^{-3})	$6.48(1) \times 10^{-22}$
DM(cm^{-3}pc)	67.93(1)
t_g (MJD)	59417.6194(2)
$\Delta\nu_p$ (s^{-1})	$1.381518(1) \times 10^{-5}$
$\Delta\dot{\nu}_p$ (s^{-2})	$-8.59(4) \times 10^{-14}$
$\Delta\ddot{\nu}$ (s^{-3})	$1.16(3) \times 10^{-21}$
$\Delta\nu_{d1}$ (s^{-1})	$3.15(12) \times 10^{-8}$
τ_{d1} (days)	6.400(2)
$\Delta\nu_{d2}$ (s^{-1})	$9.9(6) \times 10^{-8}$
τ_{d2} (days)	0.994(8)
ϕ_g	~ 0
$\Delta\nu_g/\nu$	$1.2469(5) \times 10^{-6}$
$\Delta\dot{\nu}_g/\dot{\nu}$	0.084(5)
Q_1	0.00226(9)
Q_2	0.0071(4)

glitch parameters are given in Table 3. For this analysis the white noise was characterised using `TempoNest` similarly as it was done with J1048−3832 (Sect. 3.1), obtaining $TNGlobalEF = 3.95$ and $TNGLobalEQ = -5.3$. Finally, in Fig. 5d) we show the post-fit residuals after including all the parameters in the timing model given by Eq. (2).

The glitch epoch t_g is consistent with the reports mentioned before. It can be seen t_g is accurate because $\phi_g \sim 0$. $Q_1 = 0.2(1)\%$ and $Q_2 = 0.7(1)\%$ indicates that the glitch process is dominated by the permanent jump in the frequency, as commonly detected in large glitches. We have used the values of $Q_1 = 0.2(1)\%$ and $Q_2 = 0.7(1)\%$ (fraction of glitch recovery), $\tau_1 = 6.400(2)$ and $\tau_2 = 0.994(8)$ (decay time) for this 2021 Vela glitch to compare to all other available glitches in ATNF catalog with one, two or four decay rates as displayed in Fig. 6.

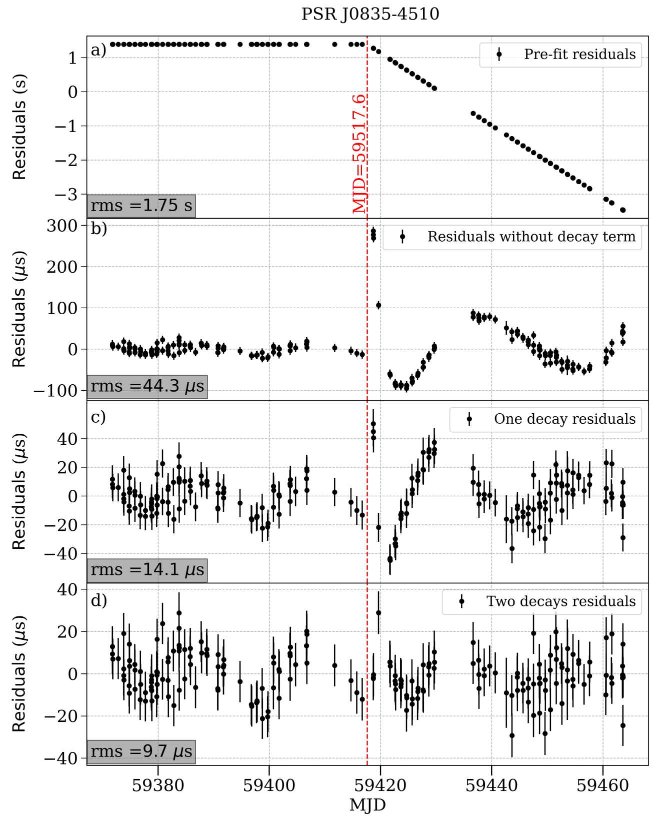

Figure 5. Vela's timing model with the parameters from Table 3.

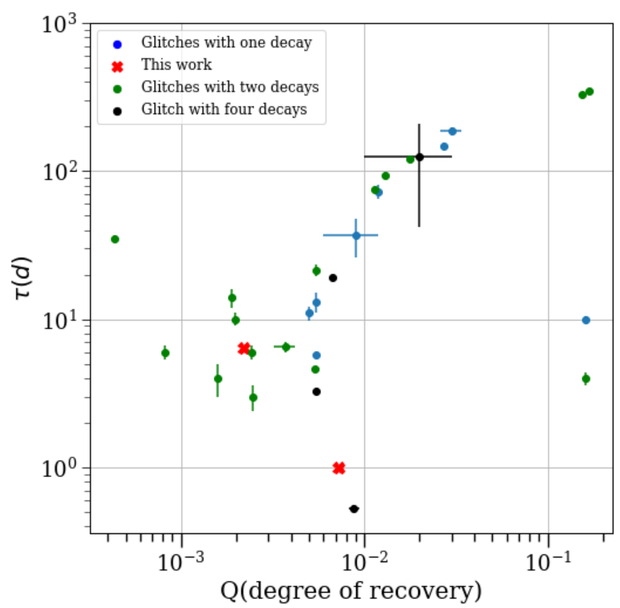

Figure 6. Comparison of current and previous glitches decaying parameters for Vela pulsar.

4 ANALYSIS METHODS: PULSE-BY-PULSE ANALYSIS OF THE 2021 VELA GLITCH

In this section we report the analysis of the observations around the Vela glitch pulse by pulse. The large amount of data is well suited for statistical and machine learning studies. Our approach has been carried out using a combination of the Variational AutoEncoder (VAE) reconstruction and the self-organizing maps (SOM) clustering techniques.

We analyze five observations on July, 19th, 20th, 21st, 23rd and 24th, 2021, performed all with antenna A1 configuration on a single polarization at 112 MHz bandwidth. The number of pulses in each observation is given in Table 4. Those are uninterrupted single observations and we supplement them with antenna A2 observation for July 20 and July 22, the day of the glitch, which are split into two and three observations respectively, as show in Table 5. All observations have been cleaned from radio frequency interferences using the code RFIClean (Maan et al. 2021) with protection of the fundamental frequency of Vela (11.184 Hz) at each of the days of observations, as described in Appendix C of Lousto et al. (2021), where we found that using `rfifind` (a task within `PRESTO` (Ransom 2018)) on the data output from `RFIClean` further improves the S/N in most of the cases. The amplitudes of the pulses are in arbitrary units as we did not monitor any reference source.

4.1 Self-Organizing Map (SOM) techniques

Here we describe a deep learning generative and clustering method built on Variational AutoEncoders (VAE) and Self-Organizing Maps (SOM) to perform Vela per-pulse clustering in an unsupervised manner. Recently, deep learning has been leveraged across many domains – from medical imaging tasks to natural language translation – with related astronomical tasks of galaxy image denoising (Chianese et al. 2020). With deep neural networks, latent representations can be learned via the hierarchical information bottlenecking intermediate layers that capture the inherent feature characteristics of the input data. From these latent representations, one can efficiently group the individual pulses into hierarchically meaningful clusters.

For the task of de-noising the pulsar signals and generating a meaningful latent representation, we resort to the popular unsupervised approach of the Variational Autoencoder, a deep learning framework that reconstructs a given input after being subjected to dimensionality regularization and stochasticity (Kingma & Welling 2014). We refer to (Lousto et al. 2021) for mathematical details and present a methodological overview instead. For each pulse, $\mathbf{x_i}$, its mean μ and standard deviation σ are generated from a neural network encoder and a latent sample $\mathbf{z_i}$ is derived from its variational (usually Gaussian) approximation $q_\phi(\mathbf{z_i}|\mathbf{x_i})$. This is then (normally) passed through an identical but reversed neural network decoder to get the reconstructed output $\hat{\mathbf{x}}_\mathbf{i}$ and the error in reconstruction is leveraged as an optimization objective. The information bottleneck allows the network to capture only the meaningful variations within the data distribution and discard any irrelevant noise. The stochasticity that the *variational* approach brings is that a regularization term in the objective function encourages the encoding network to learn a structurally meaningful latent distribution, such that 'walks' in the latent space produce coherent interpolations between points.

Once the denoising VAE is trained, we perform pulse clustering through the Self-Organizing Map (SOM), a neural network-based clustering algorithm that optimises a two-dimensional discrete map to topographically represent the input data as nodes (Kohonen 1988). It is, in essence, a generalised form of the K-Means algorithm, in which the 'centroids' exert topographical force on its neighbours whenever it is updated. The SOM consists of a 2D grid containing M nodes, $\mathcal{V} = \{v_1, v_2, ..., v_M\}$, that, for each node $v \in \mathcal{V}$, have assigned weight vectors $\mathbf{r}^v$. The grid is iteratively optimised to minimise the Euclidean distance between every input and its closest node called the Best Matching Unit (BMU) by dragging the node towards the input. To preserve the SOM's topographic structure, updated nodes pull its neighbouring nodes in its update direction - often done with a neighbourhood distance weight function that decays over the course of fitting. Training completes when the relative change in error between iterations stalls and the resulting node positions represent cluster centres (or *prototypes*) of the input and new samples can be assigned to the closest prototype.

Though both the latent representations or the original, noisy signals can be used as inputs to the SOM, we primarily consider the reconstructed signals $\hat{\mathbf{X}}$ as they are sufficient approximations to the original and minimise noise (samples are provided in Fig. 11). The schematic diagram of VAE and usage of SOM for clustering is presented in Fig. 11 of Lousto et al. (2021).

4.2 Results

We have collected the results of the SOM clustering for the five days of observation in Fig. 7. The results are displayed by days in successive rows and the three columns correspond to the choice of collecting the whole set of pulses in 4, 6, and 9 clusters respectively. The glitch on July 22nd 2021 would lie between rows 3 and 4. We have chosen the same vertical scale to represent the mean pulse of each cluster over the choices of the number of clusters and over the days of observation in order to exhibit the relative amplitudes, also affected by the different amount of observing time. The labelling of the clusters in each panel are ordered from the largest to the lowest amplitude mean pulse; while cluster 0 is the total mean pulse of the whole observation and remains the same over the three horizontal panels as a reference value. We first note an increase in the amplitude of the mean pulse of the cluster 1 as we increase the numbers of clusters allowed to SOM. They also decrease the number of pulses per cluster (as expected), what explains the increase in amplitude. This behaviour is shared by clusters 2 and 3 and successively. We also note an earlier arrival and a mild decrease in the width of the high amplitude clusters (feature that could be used for improved timing in other circumstances or for other millisecond pulsars as we noted in Lousto et al. (2021)). These points are more precisely quantified, with estimated errors, in the Tables in Appendix A.

We note that the cluster distribution follows a similar pattern to our previous studies with observations about six months before this glitch, on January 21, 24, 28 and March 29, 2021. However, the observations of July 20, two days before the glitch, show a baseline behaviour with unusual activity before and after the main pulse, which in turn decreases in amplitude relative to other neighbouring days. On the other hand this effect gets suppressed when the observation is not dissected into clusters.

In Fig. 8 we represent the sequence of pulses for each day of observation with large amount of data: 19, 20, 21, and 23 July (rows) per SOM clustering for 4, 6, and 9 clusters (columns) in blocks of ordered 5000 pulses. Those histograms provide a rough distribution over time of the clusters during each observation. The 4 clusters distribution gives a more robust view of the classes of pulses with a certain consistency over time except for the second half of the 20 July observation where there seems to be a shuffle of the high amplitude pulses into the low amplitude ones or an increase of the general noise of the signal. The 6 and 9 SOM clusters decomposition confirms

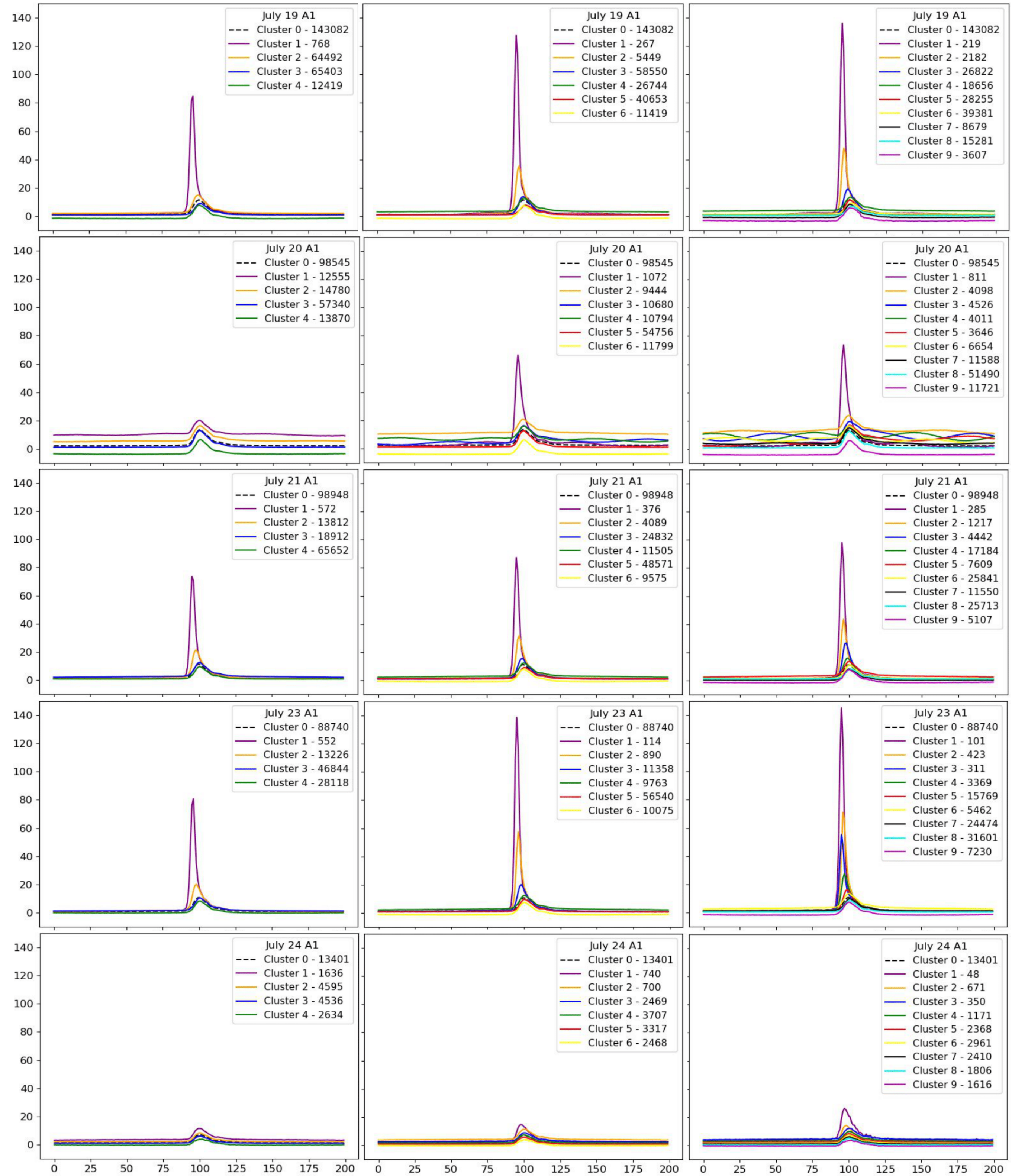

Figure 7. Mean cluster reconstruction for observations with A1 on July 19, 20, 21, 23, and 24, 2021, using 4, 6, and 9 SOM clustering.

Table 4. Date of each observation with A1, duration in hours, the MJD at the beginning and end of the observations, the corresponding number of single pulses, instantaneous topocentric period, P_{obs}, and estimated signal to noise ratio (SNR) for the selected observations around the 2021 Vela glitch used for the pulse-by-pulse analysis. The estimated time of the glitch on July 22 is MJD 59417.6194(2).

Date	Duration [h]	initial MJD	final MJD	# pulses	P_{obs} [ms]	SNR
July 19	3.55	59414.6256	59414.7737	143082	89.4142714	265.9
July 20	2.45	59415.6688	59415.7708	98545	89.4142431	241.0
July 21	2.45	59416.6656	59416.7680	98948	89.4141939	372.3
July 23	2.20	59418.6708	59418.7626	88740	89.4139894	283.3
July 24	0.33	59419.6238	59419.6377	13401	89.4139192	69.0

Table 5. Date of selected observation with A2, the MJD at the beginning and end of the observation, the corresponding number of single pulses used for the pulse-by-pulse analysis of the 2021 Vela glitch, and the initial topocentric period, P_{obs}. The estimated time of the glitch on July 22 is MJD 59417.6194(2).

Date	initial MJD	final MJD	# pulses	P_{obs} [ms]
July 22 A22	59417.65584	59417.68289	26131	89.414030
July 22 A23	59417.68317	59417.74006	54970	89.414042
July 22 A24	59417.74035	59417.76530	24117	89.414068
July 20 A21	59415.63988	59415.74171	98394	89.414230
July 20 A22	59415.74200	59415.77083	27853	89.414276

in more detail these findings. During the July 20 observation there is a transition from a high amplitude to a low amplitude dominated number of pulses that is then recovered in the posterior days of observation. The interpretation of this change in the pulse structure as a transition from a beaming dominated radiation to a more distributed or chaotic radiation over the magnetosphere of the neutron star is an interesting possibility and can be an early indicator of a coming glitch and that a re-accommodation of the magnetic field is taking place at time scales much longer than previously expected (days). Independent and new observations would be required to confirm this possibility.

4.2.1 Glitch Day: July 22 2021 observations with A2

Unlike the continuous observations with A1, those performed with A2 suffered from short (a few seconds) interruptions due to some software/hardware limitations. The observations on July 22, 2021 (the day of the glitch) are divided in three parts as described in Table 5. The first of those observations, starting at MJD 59417.65584, is about 52 minutes after the estimated occurrence of the glitch at MJD 59417.6194(2). Since those three individual sub-observations contain enough pulses to make a SOM analysis we proceed to consider them individually independent. The results of those 6 SOM clustering studies are displayed in Fig. 9.

To supplement the information in Table 5 for the observations with A2 discussed here, we have that in total the observation time on July 22 is 2.65 h (divided into three observations) with a total SNR of 689, while on July 20, the (2) observations added up to 3.14 h with a total SNR of 814.

In Fig. 9 we display the results for 6 SOM clustering for the two observations with A2 on the glitch day July 22 as described in Table 5. We first observe that the right hand side of the mean cluster pulses seem to superpose and that the sequence of clusters, with increasing amplitude seem to appear earlier and earlier. The pulse width also shows a (weak) dependence on the cluster, being narrower for higher amplitude mean pulses. All these features, for the three observations covering from roughly 1–3.5 h after this large glitch seem to be similar to those in between glitches, as we have observed in our previous analysis of the Vela pulses from January and March 2021 (Lousto et al. 2021).

4.2.2 July 20 2021 observations

The observations of July 20 present a distinctive feature with respect to the previous and posterior days to the glitch on July 22 as seen in Fig. 7. Already at the level of 4 SOM cluster analysis a baseline displacement on the mean cluster pulses is observed. From the total integration of pulses (cluster 0 labeled in this figure), it would be difficult to say something extraordinary is happening, but as we choose 6 and then 9 SOM clusters we are able to discern more details on the baseline behavior. We present a zoomed in display of the cluster distribution in Fig. 10. The oscillations appear more notable in the high amplitude clusters while those with lower amplitude seem to remain quiet. Even with the 9 cluster dissection the largest peak amplitude appears to be half of the other days, but this might well be because cluster 1 has many more pulses than during other days and this number did not decrease much with an increasing number of SOM clusters. The baseline amplitudes grows globally, indicating a potential "leakage" of the radiation from the main pulse into its nearby baseline like if a global increase of the radiation from the whole magnetosphere takes place outside the usual radio-beam.

In order to show that what we observe with the clusters baseline is not an artifact of the VAE pulse reconstruction method, in Fig. 11 we display some selected *individual* raw pulses belonging to the 4 SOM clusters versus their corresponding reconstructions showing the actual baseline fluctuations. This allow us to speculate on a direct physical interpretation of its origins in terms of the properties of the pulsar magnetosphere radiation regions.

In Fig. 12 we display the detail of the number of pulses (as given by the side bar color map representing number density) versus time (given the ordered pulse identification number from the beginning of the observation). The 9 SOM cluster decomposition shows that while the first half of the observation (∼ 1.15 hours) the distribution over the clusters follows a pattern similar to all the other days of observation, the second part of the observation (∼ 1.30 hours) displays a clear shuffle of the number pulses from the medium/high amplitude clusters towards the low amplitude ones. This was observed as an increase of the baseline radiation and interpreted as an "un-beaming" of the typical pulsar pulses. Since this effect appears only on the July 20 observation but not on the others, we may conclude that this shuffle of radiation is a transient effect. Those shuffles may occur in the following days before the glitch (and perhaps also after) but we have simply not captured them during our period of ∼ 3 hours observations. It would be interesting to follow up our analysis with other observations to verify this hypothesis.

Given the unusual effects observed with A1 on July 20 we can cross them check with the corresponding A2 observations. The observations with A2 on July 20 have a cut that split them into two observations as described in Table 5. The first part of A2 observations start earlier than the A1 observation, and the second part of the A2 observation starts roughly about the last 30% of the A1 obser-

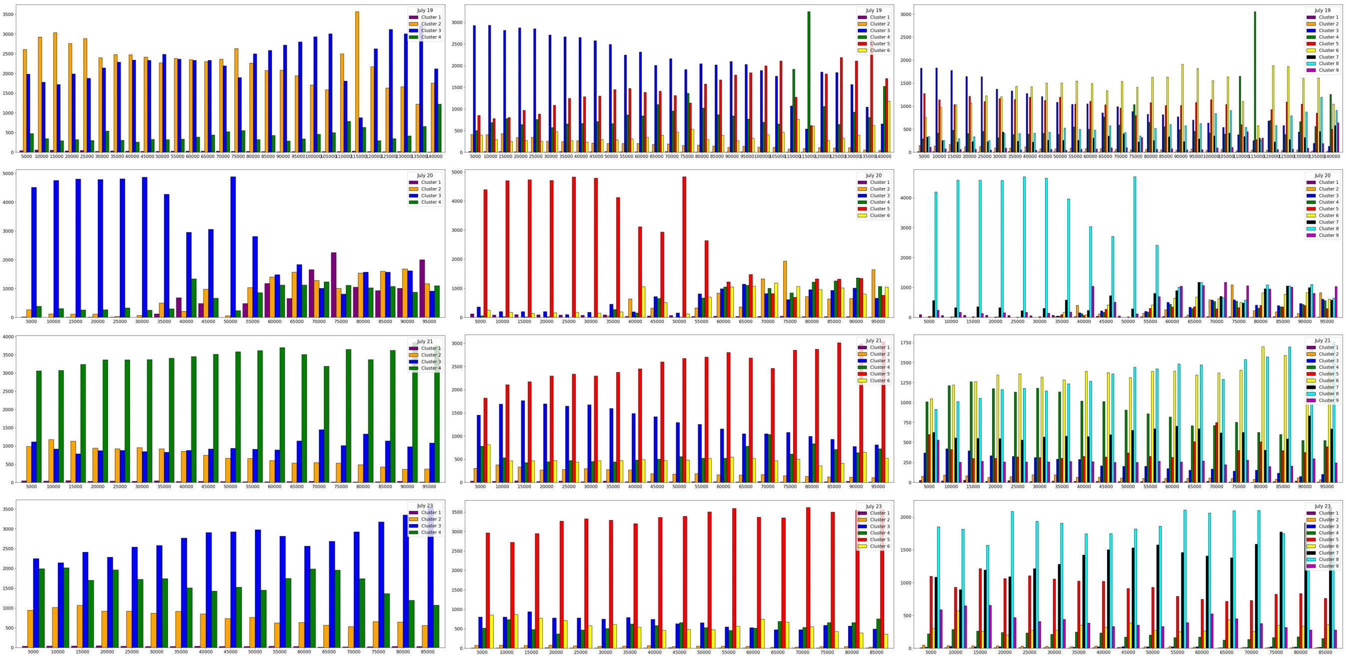

Figure 8. Time distribution by 5000 pulses of clusters for July 19,20,21,23 2021 observations on Antenna 1 for 4, 6, 9 SOM clustering.

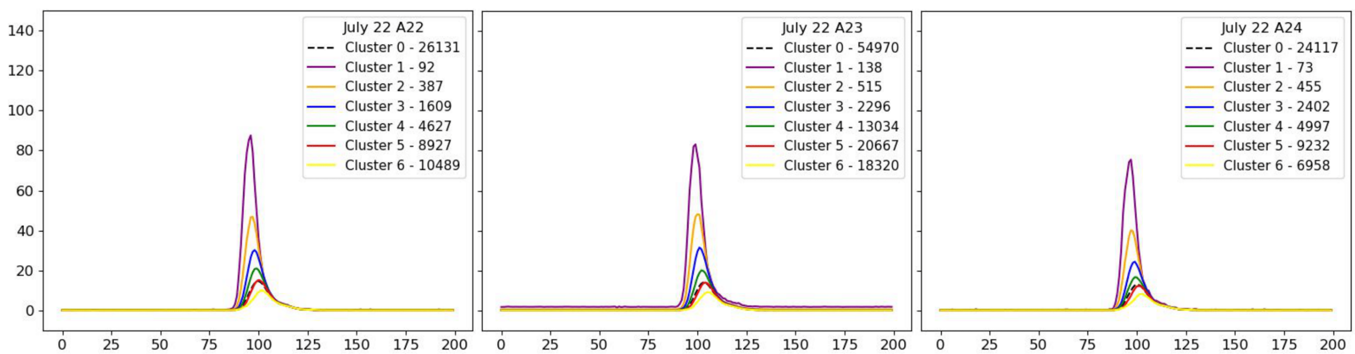

Figure 9. Mean cluster pulses for July 22 2021 three successive observations (roughly 1–3.5 h after the glitch) with Antenna 2 for 6 SOM clusters with VAE reconstruction.

vation, where the unusual effects are taking place according to our analysis in Figs. 8 and 12.

In Fig. 13 we display the Antenna 2 for 6 SOM clustering for the two observations on July 20 as described in table 5. We observe that the first observation shows the now standard pattern of mean pulses clusters ordered with increasing amplitude appearing earlier, being narrower, and a right "wing" superposition. On the other hand, the second observation shows a more shagged pulse structure, and the highest amplitude cluster displaying an increase in the baseline (noisy) emission. Since the second observation contains less pulses (27,853) than the first part (98,394) it would be expected some statistical noise, but on the other hand, we have just seen that the observation 1 and 3 with A2 of the glitch day, July 22, have less pulses but show smooth pulses structure. We can confirm now that there is a second part of the observations with A1 and A2 that display irregular features. We have not been able to discard them on the grounds of RFI or instrumental. The irregularities have different characteristics as seen with A1 or A2, but while A1 has a single polarization 112MHz bandwidth, A2 has a two (circular) polarization sensitivity with 56MHz of bandwidth. Nevertheless this potential features require further study.

5 CONCLUSIONS AND DISCUSSION

In this paper we have reported the first results of a southern glitching pulsars monitoring campaign at the Argentine Institute of Radioastronomy. In 2019 we reported a large Vela (#21 recorded) glitch Lopez Armengol et al. (2019); Gancio et al. (2020) with a $(\Delta\nu_g/\nu)_{2019} = 2.7\times10^{-6}$. Here we report a detailed analysis of the latest (#22 recorded) 2021 Vela glitch Sosa-Fiscella et al. (2021), with comparative $(\Delta\nu_g/\nu)_{2021} = 1.2\times10^{-6}$, providing an accurate description of the glitch characteristic epoch, jumps, and exponential recovery of 6.4 and 1 days times scales, (See Table 3 and Fig. 6). The accuracy of our observations and procedures allowed us to determine two mini-glitches (the smallest recorded so far) in PSR 1048−5832, (#8 and #9 recorded), with $(\Delta\nu_g/\nu)_{2020} = 8.9\times10^{-9}$

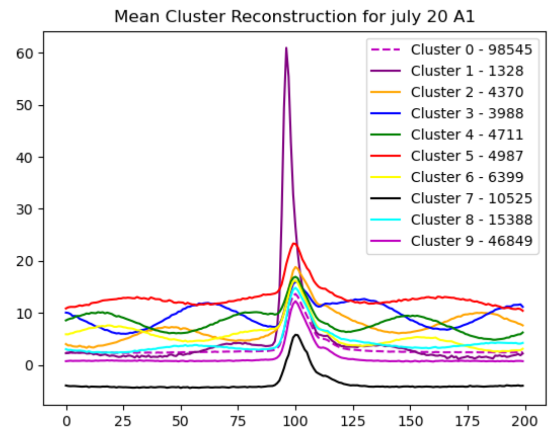

Figure 10. Mean cluster reconstruction for July 20 2021 observations on Antenna 1 for SOM 9 clustering with VAE pulses

and $(\Delta\nu_g/\nu)_{2021} = 9.9 \times 10^{-9}$, respectively. These accuracy also allowed us to make pulse-by-pulse studies of Vela and use the machine learning techniques validated in Lousto et al. (2021). Those pulse-by-pulse studies suggest that there might be indicators preceding a major glitch, a couple of days in advance, that are difficult to observe in the typical integrated folded pulse over many periods. The switch off the major pulse (and an apparent redistribution into background radiation) we see on July 20 resembles somewhat the "live" pulse analysis of the resolved 2016 Vela glitch Graber et al. (2018); Ashton et al. (2019), which can shed light on the neutron star structure and equation of state Gügercinoğlu & Alpar (2020). However our time scales for the transition seem to be much longer, of the orders of hours to days. These studies need to be expanded with new observations, what makes the Vela pulsar still an interesting source of information well after 50 years since its discovery.

With the future improvements in the antennas receivers, which include a combination of broader bandwidth and reduction of system temperature, it will be possible to study the dynamical spectra of single pulses for other pulsars of interest, such as PRS J1644−4559 and J0437-4715, the later not glitching but of interest to improve pulsar timing arrays data to detect a stochastic gravitational waves background.

ACKNOWLEDGEMENTS

We specially thank Yogesh Maan for numerous beneficial discussions about the best use of RFIClean, and Nils Andersson for discussion on the glitch theoretical modeling in regular pulsars / neutron stars. The authors also thank Cameron Knight for developing the early studies involving machine learning techniques, and Adolfo Simaz Bunzel in the observations reduction pipeline. COL gratefully acknowledge the National Science Foundation (NSF) for financial support from Grants No. PHY-1912632 and PHY-2018420 and RIT-COS 2021-DRIG grant. JAC and FG acknowledge support by PIP 0102 and PIP 0113 (CONICET). JAC and FG are CONICET researchers. JAC is a María Zambrano researcher fellow funded by the European Union -NextGenerationEU- (UJAR02MZ). This work received financial support from PICT-2017-2865 (ANPCyT). JAC was also supported by grant PID2019-105510GB-C32/AEI/10.13039/501100011033 from the Agencia Estatal de Investigación of the Spanish Ministerio de Ciencia, Innovación y Universidades, and by Consejería de Economía, Innovación, Ciencia y Empleo of Junta de Andalucía as research group FQM-322, as well as FEDER funds.

DATA AVAILABILITY

Data generated by our calculations or observations are available from the corresponding authors upon reasonable request.

REFERENCES

Abdo A. A., et al., 2009, Astrophys. J., 706, 1331
Andersson N., Glampedakis K., Ho W. C. G., Espinoza C. M., 2012, Phys. Rev. Lett., 109, 241103
Ashton G., Lasky P. D., Graber V., Palfreyman J., 2019, Nature Astronomy, 3, 1143
Basu A., et al., 2021, Monthly Notices of the Royal Astronomical Society
Chianese M., Coogan A., Hofma P., Otten S., Weniger C., 2020, Mon. Not. Roy. Astron. Soc., 496, 381
Danilenko A., Kirichenko A., Sollerman J., Shibanov Y., Zyuzin D., 2013, Astron. Astrophys., 552, A127
Dunn L., et al., 2021, The Astronomer's Telegram, 14807, 1
Espinoza C. M., Lyne A. G., Stappers B. W., Kramer M., 2011, MNRAS, 414, 1679
Fuentes J. R., Espinoza C. M., Reisenegger A., Shaw B., Stappers B. W., Lyne A. G., 2017, A&A, 608, A131
Gancio G., et al., 2020, A&A, 633, A84
Graber V., Cumming A., Andersson N., 2018, ApJ, 865, 23
Gügercinoğlu E., Alpar M. A., 2020, Mon. Not. Roy. Astron. Soc., 496, 2506
Haskell B., Melatos A., 2015, International Journal of Modern Physics D, 24, 1530008
Ho W. C. G., Espinoza C. M., Antonopoulou D., Andersson N., 2015, Science Advances, 1, e1500578
Hobbs G. B., Edwards R. T., Manchester R. N., 2006, MNRAS, 369, 655
Hotan A. W., van Straten W., Manchester R. N., 2004, Publ. Astron. Soc. Australia, 21, 302
Khomenko V., Haskell B., 2018, Publications of the Astronomical Society of Australia, 35, e020
Kingma D. P., Welling M., 2014, Auto-Encoding Variational Bayes (arXiv:1312.6114)
Kohonen T., 1988, Self-Organized Formation of Topologically Correct Feature Maps. MIT Press, Cambridge, MA, USA, p. 509–521
Lopez Armengol F. G., et al., 2019, The Astronomer's Telegram, 12482, 1
Lousto C. O., et al., 2021, Monthly Notices of the Royal Astronomical Society
Lower M. E., et al., 2021, Mon. Not. Roy. Astron. Soc., 508, 3251
Maan Y., van Leeuwen J., Vohl D., 2021, A&A, 650, A80
Manchester R. N., 2018, in Weltevrede P., Perera B. B. P., Preston L. L., Sanidas S., eds, IAU Symposium Vol. 337, Pulsar Astrophysics the Next Fifty Years. pp 197–202, doi:10.1017/S1743921317009607
Manchester R. N., Hobbs G. B., Teoh A., Hobbs M., 2005, AJ, 129, 1993
Mcculloch P., Klekociuk A., Hamilton P., Royle G., 1987, Australian Journal of Physics, 40, 725
Montoli A., Antonelli M., Pizzochero P. M., 2020, MNRAS, 492, 4837
Olney S., 2021, The Astronomer's Telegram, 14808, 1
Palfreyman J., Dickey J. M., Hotan A., Ellingsen S., van Straten W., 2018, Nature, 556, 219
Ransom S., 2011, PRESTO: PulsaR Exploration and Search TOolkit (ascl:1107.017)
Ransom S., 2018, PRESTO - Pulsar Exploration and Search Toolkit, https://www.cv.nrao.edu/~sransom/presto/
Ransom S. M., Cordes J. M., Eikenberry S. S., 2003, ApJ, 589, 911
Singha J., Joshi B. C., Arumugam P., Bandyopadhyay D., 2021, The Astronomer's Telegram, 14812, 1

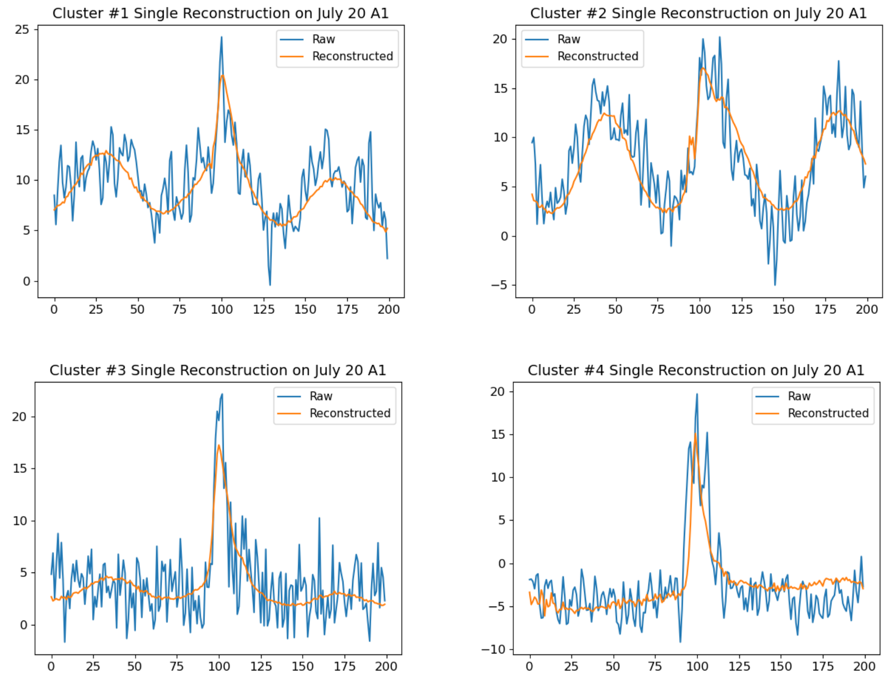

Figure 11. Sample of VAE pulse reconstruction for July 20 2021 observations with A1 for 4 SOM clustering.

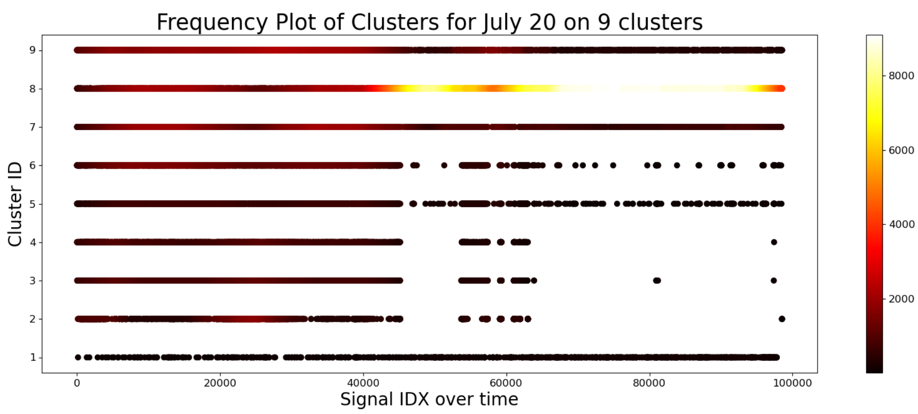

Figure 12. Time line distribution of number of pulses for the July 20 2021 observations on Antenna 1 for 9 SOM clustering.

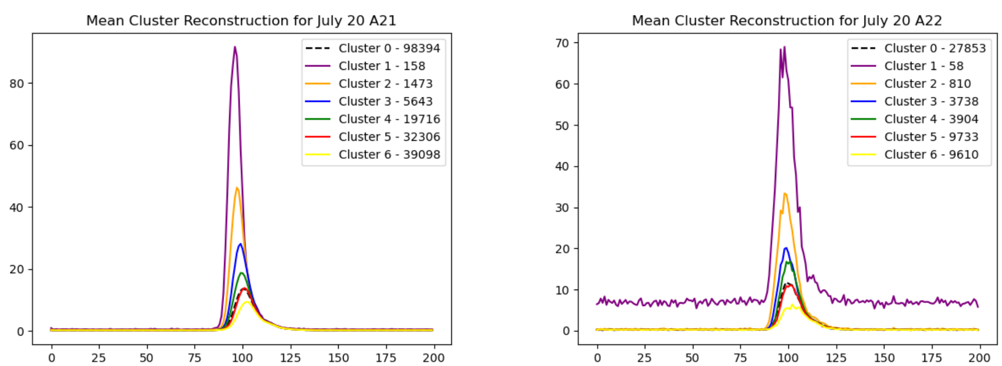

Figure 13. Mean cluster reconstruction for July 20 2021 two observations on Antenna 2 for SOM 6 clustering with VAE pulses

Sosa-Fiscella V., et al., 2021, The Astronomer's Telegram, 14806, 1

Taylor J. H., 1992, Philosophical Transactions of the Royal Society of London, 341, 117

Wang N., Manchester R. N., Pace R. T., Bailes M., Kaspi V. M., Stappers B. W., Lyne A. G., 2000, Mon. Not. Roy. Astron. Soc., 317, 843

Yan W. M., Manchester R. N., Wang N., Wen Z. G., Yuan J. P., Lee K. J., Chen J. L., 2020, Mon. Not. Roy. Astron. Soc., 491, 4634

Yu M., et al., 2013, MNRAS, 429, 688

Yuan J. P., Wang N., Manchester R. N., Liu Z. Y., 2010, MNRAS, 404, 289

Zhou Z.-R., Wang J.-B., Wang N., Yuan J.-P., Kou F.-F., Dang S.-J., 2022, arXiv e-prints, p. arXiv:2206.12886

Zubieta E., et al., 2022, Boletin de la Asociacion Argentina de Astronomia La Plata Argentina, 63, 262

APPENDIX A: TABLES OF SOM CLUSTERING

Here we include the numerical information in tabular form about the clustering analysis summarized in Fig. 7. They include a 6 SOM clusters decomposition as representative for each of the days of observation. The cluster #0 corresponds to the total number of pulses in the observation and the successive clusters from #1 to the #6 SOM clustering are ordered accordingly to the highest peak amplitude of the mean pulse computed for each cluster and represented in Fig. 7. We compute the peak location with respect to our grid of bins (here centered at around 100 for cluster #0) and totaling 1220 bins per period. We also provide a measure of the pulse mean (half) width and skew, all with estimated $1-\sigma$ errors, and finally MSE is the standard mean squared error $\sum_{i=1}^{N}(x_i-\bar{x})^2/N$, the average per-step mean squared reconstruction error over all sequences. We observe a systematic tendency for the pulses' peaks to appear earlier the higher the amplitude as well as a reduction of its width and an increase of the skew (Also observed in the previous work Lousto et al. (2021) analyzing Jan. 21, 24, 28 and March 29, 2021 observations), except for the especial case of the July 20 observations.

july22A23

This paper has been typeset from a TEX/LATEX file prepared by the author.

Table A1. SOM Clustering for July 19 with Antenna 1.

Cluster #	# Pulses	Peak Loc	Peak Height	Peak Width	Peak Skew	MSE
0	143082	100.28 ± 4.30	13.31 ± 9.81	8.23 ± 3.60	3.39 ± 0.76	0.00004 ± 0.00008
1	328	95.26 ± 0.69	129.84 ± 43.14	3.40 ± 0.34	6.84 ± 0.57	0.02966 ± 0.13766
2	6973	97.14 ± 0.99	36.52 ± 14.53	3.61 ± 0.55	4.80 ± 0.74	0.00102 ± 0.00243
3	55882	99.77 ± 1.23	14.90 ± 4.39	8.18 ± 1.26	3.65 ± 0.38	0.00011 ± 0.00020
4	17810	100.22 ± 11.30	13.71 ± 5.24	12.63 ± 5.98	2.40 ± 0.99	0.00042 ± 0.00071
5	49474	101.24 ± 1.48	8.59 ± 1.76	10.00 ± 1.05	3.31 ± 0.40	0.00012 ± 0.00019
6	12615	100.75 ± 1.56	8.40 ± 3.93	10.07 ± 1.57	3.11 ± 0.68	0.00050 ± 0.00084

Table A2. SOM Clustering for July 20 with Antenna 1.

Cluster #	# Pulses	Peak Loc	Peak Height	Peak Width	Peak Skew	MSE
0	98545	99.66 ± 15.13	15.24 ± 9.75	15.00 ± 9.45	2.33 ± 1.34	0.00008 ± 0.00019
1	1308	96.26 ± 0.76	65.79 ± 29.64	4.80 ± 0.70	4.83 ± 0.86	0.01173 ± 0.07067
2	7542	98.14 ± 26.17	23.02 ± 6.43	24.39 ± 10.35	0.67 ± 0.77	0.00136 ± 0.00239
3	10502	99.50 ± 24.69	17.97 ± 5.06	22.04 ± 10.56	0.83 ± 0.85	0.00092 ± 0.00156
4	20454	100.51 ± 17.77	16.61 ± 6.16	12.76 ± 5.91	1.73 ± 1.14	0.00044 ± 0.00079
5	47964	99.50 ± 9.51	13.36 ± 5.98	9.33 ± 1.45	2.99 ± 0.95	0.00015 ± 0.00029
6	10775	100.35 ± 3.36	6.73 ± 5.15	9.57 ± 1.38	2.79 ± 0.94	0.00068 ± 0.00118

Table A3. SOM Clustering for July 21 with Antenna 1.

Cluster #	# Pulses	Peak Loc	Peak Height	Peak Width	Peak Skew	MSE
0	98948	99.95 ± 1.59	12.84 ± 8.70	9.27 ± 1.62	3.47 ± 0.59	0.00007 ± 0.00012
1	501	95.42 ± 0.73	87.19 ± 37.85	3.60 ± 0.43	6.27 ± 0.52	0.01822 ± 0.08315
2	6121	97.02 ± 0.90	29.68 ± 10.70	5.49 ± 0.89	4.48 ± 0.51	0.00122 ± 0.00267
3	22475	98.89 ± 0.97	16.32 ± 3.14	7.42 ± 0.83	3.69 ± 0.35	0.00031 ± 0.00055
4	21361	100.73 ± 1.03	10.81 ± 1.84	9.84 ± 0.97	3.06 ± 0.56	0.00032 ± 0.00051
5	41055	100.60 ± 1.25	9.32 ± 2.10	9.69 ± 1.00	3.45 ± 0.34	0.00016 ± 0.00025
6	7435	100.04 ± 1.53	8.68 ± 3.68	9.60 ± 1.32	3.05 ± 0.60	0.00092 ± 0.00150

Table A4. SOM Clustering for July 22 with Antenna A2, Observation 1.

Cluster #	# Pulses	Peak Loc	Peak Height	Peak Width	Peak Skew	MSE
0	26131	100.15 ± 1.70	16.35 ± 8.57	9.26 ± 0.67	3.54 ± 0.25	0.00024 ± 0.00040
1	92	95.65 ± 0.50	88.78 ± 19.49	7.70 ± 0.29	4.41 ± 0.10	0.12615 ± 0.58499
2	387	96.66 ± 0.91	48.20 ± 7.94	8.39 ± 0.18	4.12 ± 0.13	0.01874 ± 0.03667
3	1609	97.92 ± 0.97	31.15 ± 3.70	8.89 ± 0.28	3.88 ± 0.12	0.00412 ± 0.00667
4	4627	98.68 ± 1.06	21.75 ± 2.76	9.51 ± 0.56	3.70 ± 0.16	0.00140 ± 0.00220
5	8927	100.00 ± 1.11	15.68 ± 2.21	9.87 ± 0.43	3.56 ± 0.17	0.00071 ± 0.00109
6	10489	101.43 ± 1.20	10.45 ± 1.61	9.91 ± 0.71	3.37 ± 0.22	0.00060 ± 0.00094

Table A5. SOM Clustering for July 22 with Antenna A23.

Cluster #	# Pulses	Peak Loc	Peak Height	Peak Width	Peak Skew	MSE
0	54970	99.76 ± 1.69	15.57 ± 7.79	9.93 ± 0.68	3.56 ± 0.20	0.00014 ± 0.00204
1	138	94.76 ± 1.08	85.77 ± 18.33	7.98 ± 1.67	4.27 ± 1.00	0.06816 ± 0.18188
2	515	96.17 ± 0.97	50.06 ± 7.30	8.21 ± 0.27	4.15 ± 0.18	0.01428 ± 0.02705
3	2296	97.17 ± 0.82	32.33 ± 3.86	8.83 ± 0.34	3.93 ± 0.10	0.00299 ± 0.00585
4	13034	98.23 ± 1.07	20.82 ± 3.07	9.58 ± 0.29	3.71 ± 0.11	0.00050 ± 0.00080
5	20667	99.82 ± 1.04	14.41 ± 1.95	10.23 ± 0.35	3.56 ± 0.11	0.00030 ± 0.00048
6	18320	101.24 ± 1.11	9.55 ± 1.45	9.88 ± 0.52	3.40 ± 0.14	0.00058 ± 0.01059

Table A6. SOM Clustering for July 22 with Antenna A2, Observation 3.

Cluster #	# Pulses	Peak Loc	Peak Height	Peak Width	Peak Skew	MSE
0	24117	100.66 ± 1.72	14.58 ± 7.34	9.71 ± 0.68	3.52 ± 0.24	0.00026 ± 0.00044
1	73	96.73 ± 0.63	76.18 ± 13.84	7.74 ± 0.36	4.39 ± 0.10	0.14697 ± 0.71118
2	455	97.49 ± 0.70	41.17 ± 6.94	8.12 ± 0.32	4.09 ± 0.11	0.01556 ± 0.03238
3	2402	98.68 ± 0.94	25.22 ± 3.33	9.29 ± 0.37	3.82 ± 0.09	0.00268 ± 0.00427
4	4997	99.29 ± 1.02	17.34 ± 2.32	9.96 ± 0.42	3.60 ± 0.14	0.00127 ± 0.00197
5	9232	100.96 ± 1.16	12.83 ± 1.95	9.87 ± 0.30	3.51 ± 0.17	0.00067 ± 0.00103
6	6958	102.19 ± 1.16	8.85 ± 1.10	10.46 ± 1.31	3.33 ± 0.19	0.00091 ± 0.00154

Table A7. SOM Clustering for July 23 with Antenna 1.

Cluster #	# Pulses	Peak Loc	Peak Height	Peak Width	Peak Skew	MSE
0	88740	100.03 ± 1.55	12.45 ± 9.27	8.13 ± 1.81	3.45 ± 0.63	0.00007 ± 0.00013
1	133	95.05 ± 0.68	141.15 ± 40.55	3.25 ± 0.29	6.94 ± 0.40	0.07106 ± 0.23160
2	1610	96.29 ± 0.82	50.89 ± 20.57	3.96 ± 0.67	5.46 ± 0.66	0.00484 ± 0.01265
3	17975	98.58 ± 1.19	17.95 ± 5.35	7.67 ± 1.38	3.84 ± 0.47	0.00038 ± 0.00071
4	6501	100.18 ± 1.40	13.78 ± 4.03	8.79 ± 1.37	2.78 ± 0.72	0.00107 ± 0.00175
5	50900	100.59 ± 1.18	9.70 ± 2.15	8.60 ± 0.85	3.40 ± 0.39	0.00012 ± 0.00020
6	11621	100.33 ± 1.35	8.47 ± 3.66	9.72 ± 1.46	3.11 ± 0.62	0.00056 ± 0.00091

Table A8. SOM Clustering for July 24 with Antenna 1.

Cluster #	# Pulses	Peak Loc	Peak Height	Peak Width	Peak Skew	MSE
0	13401	100.42 ± 1.73	7.82 ± 3.17	9.74 ± 1.27	3.23 ± 0.34	0.00052 ± 0.00256
1	424	99.73 ± 1.68	15.01 ± 4.92	8.91 ± 0.87	3.33 ± 0.30	0.02562 ± 0.42168
2	1223	98.48 ± 1.22	12.94 ± 2.46	9.27 ± 0.76	3.60 ± 0.19	0.00624 ± 0.02066
3	1622	100.71 ± 1.48	9.66 ± 1.44	9.38 ± 1.16	3.24 ± 0.24	0.00429 ± 0.00654
4	3959	100.39 ± 1.61	8.06 ± 1.49	9.77 ± 1.32	3.33 ± 0.28	0.00168 ± 0.00266
5	3292	100.46 ± 1.77	6.57 ± 1.53	9.66 ± 1.68	3.20 ± 0.33	0.00203 ± 0.00356
6	2881	101.18 ± 1.48	4.64 ± 1.05	10.61 ± 1.96	2.92 ± 0.26	0.00237 ± 0.00374